






Geo-Registration of Terrestrial LiDAR Point Clouds with Satellite Images without GNSS

Xinyu Wang[†] , *Student Member, IEEE*, Muhammad Ibrahim , Haitian Wang , *Student Member, IEEE*,
Atif Mansoor , and Ajmal Mian , *Senior Member, IEEE*

Abstract—Accurate geo-registration of LiDAR point clouds presents significant challenges in GNSS (Global Navigation Satellite System) signal denied urban areas. Existing methods typically rely on real-time GNSS and IMU (Inertial Measurement Unit) data, that require pre-calibration and assume stable positioning during data collection. However, this assumption often fails in dense urban areas, resulting in localization errors. To address this, we propose a structured geo-registration and spatial correction method that aligns 3D point clouds with satellite images, enabling frame-wise recovery of GNSS information and reconstruction of city scale 3D maps without relying on prior localization. The proposed approach employs a pre-trained Point Transformer model to segment the road points and then extracts the road skeleton and intersection points from the road point cloud as well as the target satellite image/map for alignment. Global rigid alignment of the two is performed using the intersection points, followed by local refinement using radial basis function (RBF) interpolation. Elevation correction is then applied to the point cloud based on terrain information from Shuttle Radar Topography Mission data to resolve vertical discrepancies. The proposed method was tested on the popular KITTI benchmark and a locally collected Perth (Western Australia) CBD dataset. On the KITTI dataset, our method achieved an average planimetric alignment standard deviation (STD) of 0.84 m across sequences with intersections, representing a 55.3% improvement over the original dataset. On the Perth dataset, which lacks GNSS information, our method achieved an average STD of 0.96 m compared to the GPS data extracted from Google Maps API. This corresponds to a 77.4% improvement from the initial alignment. Our method also resulted in elevation correlation gains of 30.5% on the KITTI dataset and 50.4% on the Perth dataset.

Index Terms—LiDAR, Point Cloud, Geo-registration, Skeletonization, Elevation Maps, Spatial Correction.

I. INTRODUCTION

THE rapid development of urban environments drives a growing demand for detailed 3D spatial data to support urban planning, infrastructure monitoring, and intelligent transportation systems [1], [2], [3], [4], [5], [6]. Light Detection and Ranging (LiDAR) technology is the most prevalent method for capturing high-resolution 3D point clouds, providing rich spatial representations of buildings, roads, bridges, vegetation, and other urban structures [2], [7], [8]. 3D point clouds enable a wide range of applications, including infrastructure assessment, emergency response planning, and autonomous driving [9], [10], [11].

Although significant advancements in point cloud modeling methods such as Iterative Closest Point (ICP) algorithm variants [12], [13], [14], LiDAR Odometry and Mapping (LOAM)

[15], [16], [17], and Simultaneous Localization and Mapping (SLAM) [18], [19] approaches have enabled the generation of city-scale models (e.g., Waymo Dataset [20], Perth CBD dataset [21], Swan 3D Point Cloud dataset [22]), these models are often generated without precise geographic referencing. This is largely due to limitations in the data acquisition process, where LiDAR systems collect data without a GNSS, or the GNSS and IMU sensor accuracy is compromised in urban environments [16], [23]. Factors such as signal occlusion caused by tall buildings [24], [25], sensor desynchronization [26], [27], and inconsistent sampling rates between devices [28] contribute to inaccurate or missing geographic metadata [11]. Re-capturing data to fill in missing information is expensive and time consuming [29], [30] making post-hoc geo-registration a much more preferred alternative [31].

The absence of precise georeferencing prevents the integration of point cloud models with standardized spatial coordinate systems, such as the World Geodetic System 1984 (WGS-84) and Universal Transverse Mercator (UTM) [32], [33]. This deficiency significantly limits their integration with Geographic Information Systems (GIS), hindering multi-source spatial data fusion and comprehensive spatial analysis [34], [35], [32]. Consequently, point cloud models often contain inherent spatial errors such as frame drift, global deformation, and loop closure failures [34], [36]. Without accurate geographic referencing, these errors cannot be quantitatively verified or effectively corrected, limiting the reliability and practical utility of city scale 3D models.

Several technical and environmental factors make precise geographic referencing in LiDAR-generated point clouds challenging. First, most commercial LiDAR devices such as Ouster OS0/1/2, Velodyne HDL series, and RIEGL VUX scanners, operate independently of global navigation satellite systems (GNSS), producing data in local coordinate frames without global spatial context [37]. Second, significant discrepancies exist between LiDAR devices and GNSS sensors, including differences in sampling frequency, data synchronization difficulties, and varying spatial resolution, resulting in systematic incompatibilities and misalignments [11], [23], [37]. Furthermore, many existing urban 3D point cloud datasets were initially captured without integrated GNSS information due to constraints such as signal occlusion in dense urban environments (the "urban canyon effect") [18], [38]. Considering the substantial resources and time invested in collecting high-density, high-quality point cloud data, discarding these datasets merely due to missing georeferencing information is impractical [29]. Thus, a robust methodology capable of precise geo-

All authors are with the Department of Computer Science and Software Engineering, The University of Western Australia, Perth, WA 6009, Australia. Corresponding author: frank.wang@uwa.edu.au

registration and subsequent spatial correction using existing non-georeferenced point cloud data is urgently required. Accurate geographic alignment is crucial for improving spatial accuracy and integration, as it helps mitigate typical issues such as frame drift, loop closure errors, and localized structural distortions.

To address these issues effectively, this paper introduces a structured Geo-Registration and Spatial Correction framework integrating topology-driven skeleton extraction, spatial transformations, and elevation correction. The proposed method initiates with semantic segmentation to isolate road points from raw LiDAR point cloud data. These segmented road points are projected onto a two-dimensional plane to generate a precise skeleton representation of the road network. In parallel, high-resolution satellite-derived maps undergo segmentation and skeletonization, producing corresponding road skeletons and intersection keypoints. Alignment between these skeletonized representations proceeds in two hierarchical stages: initially, rigid global alignment is achieved by matching intersection-based keypoints, establishing spatial consistency across two modalities. Subsequently, a non-rigid transformation employing radial basis function (RBF) interpolation addresses local spatial distortions, refining alignment precision at a finer scale. Finally, terrain-aware elevation adjustment corrects vertical discrepancies between the point cloud and the GIS-derived elevation model, ensuring full three-dimensional spatial coherence. Experimental validation on the KITTI datasets and Perth CBD 2021 demonstrates the efficacy of the methodology, with observed average deviation reductions of approximately 55.3% in KITTI dataset from 1.88m to 0.84m.

The primary contributions of this research are as follows:

- 1) A new problem is introduced: geo-registering terrestrial point clouds in the absence of reliable GNSS, targeting practical challenges where accurate positioning is unavailable and data re-collection is not feasible.
- 2) Cross-modal matching is enabled by extracting road features from both LiDAR point clouds and satellite imagery, producing unified skeleton representations that emphasize critical geometric structures such as intersections and road centerlines.
- 3) The proposed geo-registration framework employs a two-stage strategy, combining global rigid alignment through intersection matching and local non-rigid refinement using radial basis functions, followed by elevation correction using external terrain data.
- 4) An evaluation framework for geo-registering terrestrial point cloud is established, incorporating terrain-aware vertical adjustment and a correlation-based metric to quantify elevation consistency between point clouds and satellite-derived elevation references.
- 5) This method reveals and quantifies geo-registration errors in the KITTI dataset, resulting in a sub-dataset with corrected spatial discrepancies for selected sequences that may facilitate future benchmarking and analysis.

The remainder of this paper is organized as follows: Section II reviews related work on 3D point cloud processing and geo-registration methods. Section III details the proposed method-

ology, outlining the semantic segmentation process, skeleton extraction, and hierarchical alignment approach. Section IV presents experimental results, evaluating the performance and effectiveness of our method across various datasets. Section V discusses the practical implications, potential limitations, and avenues for future research. Finally, Section VI concludes the paper.

II. LITERATURE REVIEW

THE accurate geo-registration of urban LiDAR point clouds remains a significant challenge due to sensor limitations, urban occlusions, and the absence of reliable GNSS information. Existing research has mainly focused on three key aspects: similar approaches, road feature extraction, 3D-2D registration, and non-rigid correction methods.

A. Similar approaches

Current approaches for GPS coordinate annotation of urban point cloud datasets primarily rely on multi-sensor fusion techniques that integrate GNSS with LiDAR and IMU data [11], [23] during the collection. However, these methods face limitations in urban environments due to the "urban canyon effect" [38], where signal occlusion degrades GNSS accuracy [18]. Alternative approaches include 3D map-based global localization (MGL) using pre-existing 3D maps [37], which requires pre-constructed 3D point cloud maps for the corresponding mapping area. Additionally, SLAM-based methods that operate independently in GNSS-denied environments [15], [16] have been developed. While these techniques can provide relative positioning accuracy, they struggle with absolute georeferencing without external reference constraints.

B. Road Feature Extraction

Semantic segmentation and feature extraction from LiDAR point clouds have advanced through both classical and deep learning methods. Early works [39], [40] applied geometric and radiometric cues, while more recent studies employ neural architectures such as PointNet++ [41] and Point Transformer [42] to segment road surfaces and urban structures. Skeletonization and thinning techniques [43], [44] have been used to capture road centerlines and intersection topology, providing a concise and stable basis for spatial alignment.

C. 3D-2D Registration Techniques

Cross-modality registration approaches between 3D point clouds and 2D reference maps fall into projection-based and feature correspondence categories. Projection-based methods [45], [46] transform 3D point clouds into 2D representations for direct alignment with map imagery, but often discard useful geometric information. Feature-based techniques [47], [48] extract salient features such as intersections or building footprints to establish correspondences across modalities. However, most require either coarse initial alignment or ground control points, which limits automation and scalability in large, GNSS-denied urban environments.

D. Non-Rigid Transformation and Correction

Rigid alignment corrects global misalignments but cannot address local geometric distortions inherent to mobile LiDAR mapping. Radial basis function (RBF) methods, such as thin-plate splines [49], [50], enable continuous non-rigid warping guided by control points, and have been applied in limited urban contexts [51], [52]. The selection of topological control points, such as road intersections, is critical to preserving spatial coherence during non-rigid correction.

E. Evaluation and Benchmarking

Assessment of geo-registration accuracy in the absence of GNSS ground truth remains an open problem. Existing benchmarks focus primarily on small-scale or building-level datasets [53], [54]. Quantitative metrics based on road center-line distances and intersection offsets [55], [56] offer practical alternatives for urban-scale evaluation but lack standardization across studies.

Current methods face persistent limitations: reliance on GNSS or manual intervention, sensitivity to urban occlusion and topological abstraction, and inadequate handling of local distortions in 3D–2D registration. There is a clear need for a fully automatic, topology-driven framework that achieves robust urban geo-registration and correction using only LiDAR and map data, and can be rigorously evaluated on urban-scale datasets. Our work addresses these gaps with a unified approach combining semantic segmentation, skeleton-based topology matching, hierarchical transformation, and standardized quantitative assessment.

III. METHODOLOGY

THIS section outlines the complete pipeline designed for high-precision geo-registration of large-scale urban 3D point cloud data without reliance on GNSS information. The proposed framework consists of four principal stages: (1) pre-processing of raw LiDAR point clouds to extract road surface structures and generate a robust skeleton representation; (2) extraction and refinement of reference map data to produce a topologically consistent 2D road network skeleton and associated elevation information; (3) hierarchical alignment, which includes feature-based rigid transformation to achieve global spatial correspondence, followed by non-rigid warping using radial basis functions for local geometric correction; and (4) terrain-aware elevation adjustment to ensure vertical consistency with geographic reference data. Each component is specifically tailored to address the unique challenges associated with urban data, such as spatial noise, complex road topology, and map–point cloud domain discrepancies. The following subsections describe each stage in detail, as summarized in Figure 1.

A. 3D LiDAR Point Cloud Preprocessing

The geo-registration of large-scale urban 3D point cloud models without GNSS information requires a robust pre-processing pipeline to isolate road surface points and generate

a skeletonized network suitable for map alignment. Our approach comprises five main stages: semantic segmentation, adaptive voxel downsampling, local outlier removal, disconnected clusters filtering and skeletonization via 2D projection.

1) *Semantic Segmentation of Road Surfaces*: We first employ Point Transformer V2 [57] for semantic segmentation to extract road surface points from the raw point cloud. This architecture integrates a vector self-attention mechanism that dynamically captures local geometric relationships. For a point x_i , the vector self-attention output is:

$$\text{VSA}(x_i) = \sum_{j \in N(i)} \rho(\phi(x_i) - \psi(x_j) + \delta_{ij}) \odot \gamma(x_j) \quad (1)$$

where $N(i)$ denotes the set of neighbors for point i , ϕ , ψ , and γ are learnable mappings, δ_{ij} encodes relative positional information, ρ is a nonlinear normalization function, and \odot is element-wise multiplication. This formulation enables the network to model spatial context and aggregate relevant features for accurate road surface segmentation. The output is a binary label per point indicating road versus non-road classes.

2) *Adaptive Voxel Downsampling*: To reduce computational complexity and maintain structural fidelity, we apply adaptive voxel downsampling to the segmented road point cloud. The voxel size s is determined by:

$$s = \alpha \cdot \left(\frac{\text{vol}(P)}{|P|} \right)^{1/3} \quad (2)$$

where $\text{vol}(P)$ is the volume of the point cloud's bounding box, $|P|$ is the number of points, and α is an empirically set scaling factor. The point cloud is partitioned into voxels of size s , and one representative point per voxel is retained. This operation preserves essential geometric details while significantly reducing the data volume.

3) *Local Outlier Removal*: Residual noise and isolated points can degrade downstream processing. To mitigate this, we perform a local statistical outlier removal procedure. For each point p_i , we compute the average distance μ_i and the standard deviation (std) σ_i to its k nearest neighbors ($k = 20$). A point is classified as an inlier if:

$$\text{is_inlier}(p_i) = (\mu_i + \beta \cdot \sigma_i) < \tau(p_i) \quad (3)$$

where β is a fixed threshold (typically 2.5) and $\tau(p_i)$ is a spatially adaptive distance threshold based on the local density. This criterion effectively removes outliers that do not conform to the local spatial distribution of the point cloud.

4) *Density-Based Cluster Filtering*: After local outlier removal, the point cloud may still contain small, disconnected clusters arising from occlusions or artifacts. We utilize DBSCAN (Density-Based Spatial Clustering of Applications with Noise)[58] to identify and retain only the main road structures. For each point p_i , the neighborhood radius ϵ_i is adaptively set as:

$$\epsilon_i = \gamma \cdot \frac{1}{k} \sum_{j=1}^k \|p_i - p_j\| \quad (4)$$

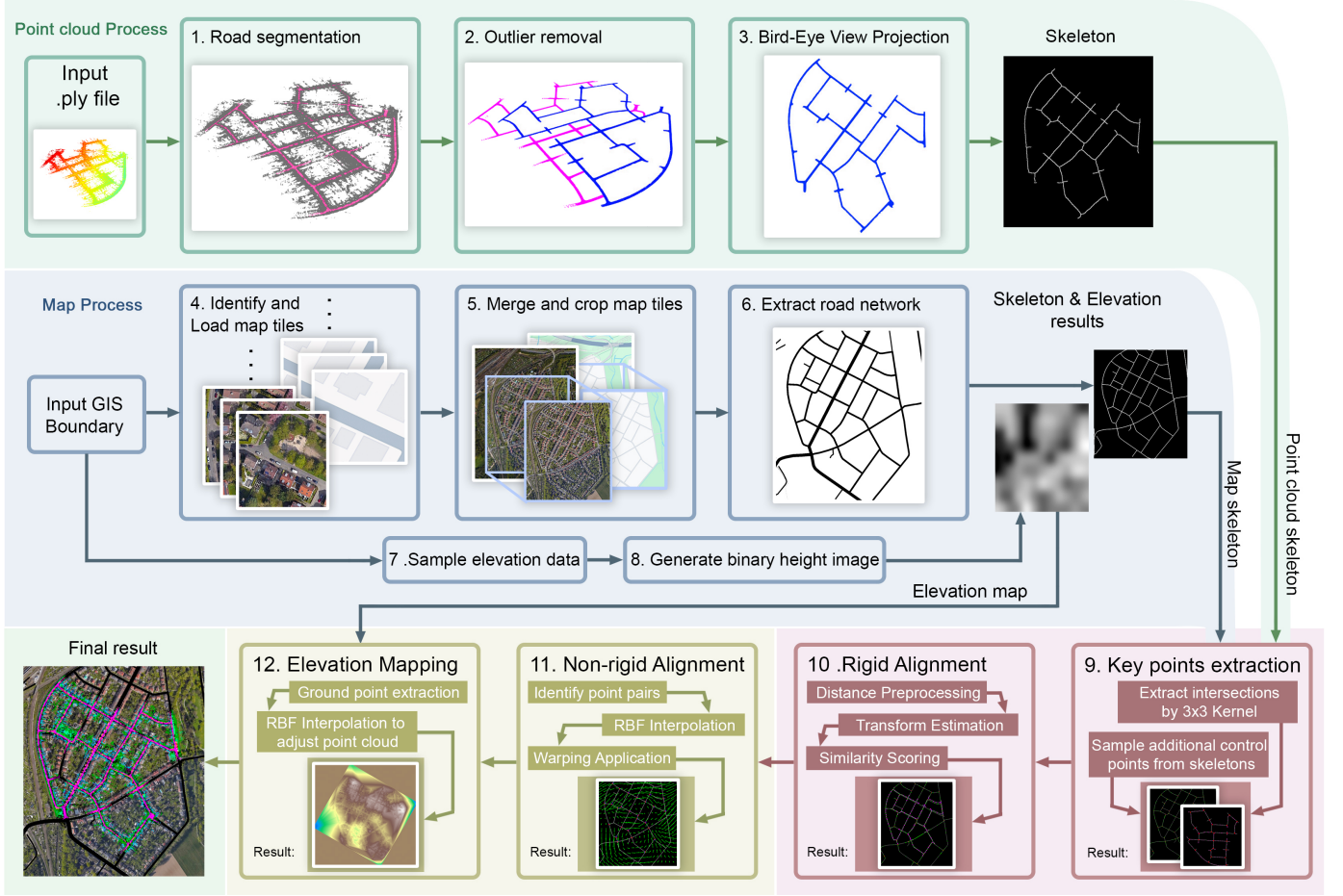


Fig. 1. 1) Point cloud processing contains road segmentation, outlier removal, and 2D projection to generate skeleton results from .ply file inputs. 2) Map processing contains map tile identification and loading, merging and cropping tiles, road network extraction, and elevation data sampling to generate skeleton and height maps. 3) Rigid alignment includes distance preprocessing, transform estimation, and similarity scoring to establish initial correspondence between point cloud and map skeletons. 4) Non-rigid alignment and elevation matching include point pair identification, RBF interpolation, warping application, ground point extraction, and RBF interpolation to adjust the point cloud, resulting in the final aligned point cloud.

where γ is a scaling factor (set to 1.8) and k is the number of nearest neighbors used for local density estimation. Clusters with fewer than $\text{minPts} = 17$ points are removed. This step eliminates fragmented and low-density regions, further refining the road network.

5) *2D Projection and Skeletonization*: The denoised road point cloud is then projected onto the XY -plane to create a 2D representation. For each 3D point (x, y, z) , only (x, y) is retained. We apply iterative morphological thinning to extract the road centerline skeleton S . The skeletonization process iteratively removes peripheral pixels from $I(x, y)$ while preserving the topological structure, producing a single-pixel-wide network that maintains road connectivity, especially at intersections. Short spurious branches are pruned using:

$$S_{\text{pruned}} = S \setminus \{p \in S \mid d_{\text{endpoint}}(p) < L_{\min} \wedge \kappa(p) < \kappa_{\text{th}}\} \quad (5)$$

where $d_{\text{endpoint}}(p)$ is the distance from p to the nearest skeleton endpoint, $\kappa(p)$ is the local curvature, L_{\min} is a minimum branch length, and κ_{th} is a curvature threshold. This produces a robust topological graph, providing the necessary foundation for subsequent map alignment.

B. 2D Reference Map Preprocessing

Accurate geo-registration of urban 3D point clouds requires that both the input point cloud and the reference map share a comparable and topologically consistent road network representation. To achieve this, we process high-resolution reference maps to extract a 2D skeletonized road network suitable for feature-based alignment with the point cloud.

1) *Acquisition of Reference Maps*: We obtain georeferenced satellite imagery and vector road network data for each study region using the Google Maps API with the Mercator projection, ensuring uniform spatial resolution and a well-defined coordinate reference system. The initial map data, however, is unsuitable for direct alignment due to abstraction artifacts: road widths are stylized, semantic content is simplified, and map data often contains topological inconsistencies.

2) *Color-Based Segmentation*: To extract the road mask from map imagery, we convert the RGB satellite map to the HSV color space and perform thresholding to isolate the road regions, which typically appear as high-value (near-white) areas. Let $I_{\text{HSV}}(x, y)$ denote the pixel at (x, y) in HSV color space. The binary road mask M_{init} is set to 1 where $H_{\min} \leq H(x, y) \leq H_{\max}$, $S(x, y) \leq S_{\text{th}}$, and $V(x, y) \geq V_{\text{th}}$,

and 0 otherwise, where H, S, V denote the hue, saturation, and value channels, and the thresholds ($H_{\min}, H_{\max}, S_{\text{th}}, V_{\text{th}}$) are empirically set for each region based on the color distribution of road surfaces.

3) *Bidirectional Connected Component Filtering*: The raw road mask frequently contains isolated noise, fragmented segments, and non-road regions due to imaging artifacts or semantic mismatches. We apply connected component analysis to both the foreground (road) and background (non-road) regions. For each connected component S_i (foreground) and B_j (background), we calculate the component area and filter components below a size threshold proportional to the mean component area \bar{S} . The filtered road mask is thus:

$$M_{\text{filtered}} = \bigcup_{i: |S_i| \geq \beta \bar{S}} S_i \cup \bigcup_{j: |B_j| \geq \beta \bar{S}} B_j \quad (6)$$

where β is a tunable parameter that controls the minimal preserved component size, and $|\cdot|$ denotes the area (pixel count) of each component. This dual filtering step removes both small disconnected road artifacts and small holes within larger road segments, preserving the dominant network topology.

4) *Skeletonization and Topology Refinement*: To enable topological matching with the processed point cloud, we apply a morphological thinning algorithm to the filtered binary road mask, reducing each road segment to its centerline skeleton, $S_{\text{map}} = \mathcal{T}(M_{\text{filtered}})$, where \mathcal{T} denotes the iterative thinning operation that preserves connectivity and reduces lines to single-pixel width.

To further refine the extracted skeleton, we prune spurious short branches and artifacts that could impact downstream alignment. For each branch $b \subset S_{\text{map}}$, we evaluate its length L_b and mean local curvature κ_b . Branches satisfying $L_b < L_{\min}$ and $\kappa_b < \kappa_{\text{th}}$ are removed. The final map skeleton is:

$$S_{\text{map}}^* = S_{\text{map}} \setminus \bigcup_{b \in \mathcal{B}} \{b : L_b < L_{\min} \wedge \kappa_b < \kappa_{\text{th}}\} \quad (7)$$

where \mathcal{B} is the set of all branches in the skeleton, L_{\min} is the minimum length, and κ_{th} is the curvature threshold.

C. Rigid Alignment based on the Feature Extraction

Establishing robust correspondences between point cloud data and reference maps is a central challenge in geo-registration, due to differences in dimensionality, scale, and abstraction. Our approach addresses this challenge through a systematic feature extraction and rigid alignment framework, ensuring both global and local spatial consistency.

1) *Keypoint Detection and Construction*: Distinctive and repeatable keypoints are essential for effective map-to-point cloud alignment. In both the skeletonized point cloud and map network, we extract three types of keypoints based on intrinsic road network topology:

- 1) *Intersection points* where multiple road segments meet, identified by analyzing the local connectivity of the skeleton graph. For each skeleton pixel p in S_{pc} , we consider the 3×3 neighborhood $\mathcal{N}_{3 \times 3}(p)$, and select p as an intersection if more than two skeleton branches connect:

$$I_{pc} = \{p \in S_{pc} : |\mathcal{N}_{3 \times 3}(p) \cap S_{pc}| > 2\} \quad (8)$$

- 2) *Control points* sampled at regular intervals along each skeleton branch, ensuring even spatial coverage and enabling alignment of elongated segments. The sampling density is empirically set to 20.
- 3) *Corner points* corresponding to the geometric boundary of the skeletonized image, providing global reference for orientation and scale.

The union of these keypoints encapsulates both the topological and geometric structure of the road network, facilitating stable and repeatable correspondence search.

2) *Rigid Transformation Estimation*: Given the keypoint sets \mathcal{P}_1 (from the point cloud) and \mathcal{P}_2 (from the reference map), we perform pairwise matching to estimate the optimal similarity transformation, comprising scaling, rotation, and translation. For each candidate correspondence between point pairs $(p_i^1, p_k^1) \in \mathcal{P}_1$ and $(p_j^2, p_l^2) \in \mathcal{P}_2$, the scale factor s is computed as:

$$s = \frac{\|p_k^1 - p_i^1\|}{\|p_l^2 - p_j^2\|} \quad (9)$$

The rotation angle θ is determined by the relative orientation of the pairs:

$$\theta = - \left[\arctan 2(p_k^1[1] - p_i^1[1], p_k^1[0] - p_i^1[0]) - \arctan 2(p_l^2[1] - p_j^2[1], p_l^2[0] - p_j^2[0]) \right] \quad (10)$$

The corresponding rotation matrix is:

$$\mathbf{R}_\theta = \begin{bmatrix} \cos \theta & -\sin \theta \\ \sin \theta & \cos \theta \end{bmatrix} \quad (11)$$

A translation vector \mathbf{t} is also estimated.

The full transformation is applied to \mathcal{P}_2 :

$$\mathcal{T}'(p) = s \cdot \mathbf{R}_\theta(p - p_j^2) + p_i^1 + \mathbf{t} \quad (12)$$

3) *Proximity-Based Matching Score and Optimization*: To quantitatively evaluate each candidate transformation, we introduce a proximity-based matching score. For all transformed keypoints, we compute the minimal Euclidean distance to the corresponding set, with the score defined as:

$$S = \alpha \sum_{i=1}^{|\mathcal{P}_1|} \mathbb{I} \left(\min_j \|p_i^1 - \mathcal{T}'(p_j^2)\| < \epsilon \right) \quad (13)$$

$$+ \beta \sum_{i=1}^{|\mathcal{A}_1|} \mathbb{I} \left(\min_j \|a_i^1 - \mathcal{T}'(a_j^2)\| < \epsilon \right) \quad (14)$$

where \mathbb{I} is the indicator function, ϵ is the distance threshold, and α and β are weights for primary and auxiliary keypoint sets. The optimal parameters $(s^*, \theta^*, \mathbf{t}^*)$ maximize this score:

$$(s^*, \theta^*, \mathbf{t}^*) = \arg \max_{s, \theta, \mathbf{t}} S(s, \theta, \mathbf{t}) \quad (15)$$

4) *Global Point Cloud Transformation*: With the optimal parameters, the entire point cloud is aligned to the reference map. The transformation is implemented in a centering and rescaling framework:

$$\mathbf{p}_c = \mathbf{p} - \mathbf{c} \quad (16)$$

$$\mathbf{p}' = \mathbf{R}_{\theta^*}(s^* \mathbf{p}_c) + \mathbf{c} - \mathbf{t}^* \quad (17)$$

where \mathbf{c} denotes the centroid. This operation ensures that both local structures and global layout are spatially consistent, providing a strong initial alignment for subsequent non-rigid refinement.

D. Non-rigid Transformation Using Radial Basis Functions

While rigid alignment establishes an initial correspondence between the point cloud and the reference map, it does not account for non-uniform distortions and local spatial inconsistencies inherent in large-scale urban data acquisition. To address these residual misalignments, we introduce a non-rigid transformation step based on radial basis function (RBF) interpolation, enabling smooth and continuous warping of the point cloud to better conform to the reference map topology.

1) *Construction of the Deformation Field*: Let $\{\mathbf{s}_i\}_{i=1}^n$ and $\{\mathbf{t}_i\}_{i=1}^n$ denote matched keypoints from the point cloud skeleton and map skeleton, respectively. The non-rigid deformation field $\mathbf{f}(\mathbf{x})$ is modeled as:

$$\mathbf{f}(\mathbf{x}) = \sum_{i=1}^n \mathbf{w}_i \phi(\|\mathbf{x} - \mathbf{c}_i\|) + \mathbf{P}(\mathbf{x}), \quad (18)$$

where $\mathbf{c}_i = \mathbf{s}_i$, \mathbf{w}_i are weight vectors determined by solving the system of equations induced by the displacements $\mathbf{t}_i - \mathbf{s}_i$, $\phi(\cdot)$ is the chosen radial basis function, and $\mathbf{P}(\mathbf{x})$ is a polynomial for global affine adjustment.

We employ the thin plate spline (TPS) kernel for its smoothness properties:

$$\phi(r, \epsilon) = (r^2 + \epsilon^2)^{1/2}, \quad (19)$$

with ϵ as a regularization parameter, set to 0.6 for the main transformation and 1.0 for visualization purposes.

2) *Control Point Selection and Correspondence*: Corresponding control points are established via nearest neighbor search within a spatial threshold $\tau = 30$:

$$\mathcal{C} = \left\{ (\mathbf{s}_i, \mathbf{t}_i) \mid \mathbf{t}_i = \arg \min_{\mathbf{t} \in \mathcal{T}} \|\mathbf{s}_i - \mathbf{t}\|, \|\mathbf{s}_i - \mathbf{t}_i\| < \tau \right\}. \quad (20)$$

The resulting displacement field is computed separately for x and y directions by fitting RBF interpolators to the control point displacements.

3) *Application of Non-rigid Transformation*: The non-rigid transformation $\mathbf{f}(\mathbf{x})$ is then applied to all points in the point cloud, enabling local geometric correction while preserving global structural relationships. This process yields a spatially coherent alignment that accurately reflects both large-scale and fine-grained topological features present in the reference map.

E. Terrain-aware Elevation Matching

Accurate vertical registration is essential for integrating the aligned point cloud into geographic information systems and for maintaining geometric fidelity across varied urban landscapes. Following horizontal alignment, we implement a terrain-aware elevation correction procedure to reconcile the vertical position of points with reference terrain heights.

1) *Ground Point Extraction and Grid-based Modeling*: Ground points are segmented from the point cloud using RANSAC-based plane fitting, employing an initial height threshold $\tau_h = 0.05$ and iteratively refined to $\tau_{\min} = 0.02$. For each grid cell (x, y) with resolution $r = 1.0$, the mean ground elevation is computed as:

$$h(x, y) = \frac{1}{|S_{x,y}|} \sum_{p \in S_{x,y}} z_p, \quad (21)$$

where $S_{x,y}$ denotes ground points within the cell and z_p their respective elevations.

2) *Integration with Reference Terrain Data*: Absolute terrain heights are sourced from the prepared reference map, enabling precise assignment of global elevation values. For each ground point, its vertical coordinate is directly adjusted to match the terrain height at (x, y) . For non-ground points (e.g., buildings, vegetation), the relative height above the local ground surface is preserved by adding the original elevation offset to the terrain reference value.

3) *Outlier Suppression and Local Consistency*: To further ensure vertical consistency, a statistical filter is applied to the grid-based model. Points are flagged as outliers if their elevation deviates significantly from the mean within the local grid cell:

$$\mathcal{O} = \{p \in G : |z_p - \mu_{S_{x,y}}| > 2.5 \cdot \max(\sigma_{S_{x,y}}, \tau_{\min}/2)\}, \quad (22)$$

where $\mu_{S_{x,y}}$ and $\sigma_{S_{x,y}}$ are the mean and the std of heights in the cell. This robust filtering suppresses artifacts while ensuring the final elevation profile faithfully reproduces underlying terrain features.

F. Registration Evaluation Metrics

Despite the progress in urban point cloud geo-registration, there remains a lack of universally accepted quantitative metrics for evaluating registration accuracy in the absence of GNSS or ground truth. In this section, We introduce two methods for objective assessment: road centerline distance analysis and intersection offset evaluation. Both leverage the geometric correspondence between the aligned point cloud and the road network extracted from reference maps.

1) *Road Centerline Distance Analysis*: For each trajectory point $p_i \in \mathbb{R}^2$ in the registered point cloud, we compute its shortest perpendicular distance to the nearest road centerline segment $s_j = (\mathbf{a}_j, \mathbf{b}_j)$, where $\mathbf{a}_j, \mathbf{b}_j \in \mathbb{R}^2$ denote the segment endpoints. The direction vector of the segment is $\vec{v}_j = \mathbf{b}_j - \mathbf{a}_j$, and the unit direction vector is $\hat{v}_j = \vec{v}_j / \|\vec{v}_j\|$.

The perpendicular distance $d_{\perp}(p_i, s_{j^*})$ is given by

$$d_{\perp}(p_i, s_{j^*}) = \frac{\|\vec{v}_{j^*} \times (p_i - \mathbf{a}_{j^*})\|}{\|\vec{v}_{j^*}\|} \quad (23)$$

where s_{j^*} is the centerline segment closest to p_i in terms of orthogonal projection. More precisely, for each p_i , we identify $j^* = \arg \min_j d_{\perp}(p_i, s_j)$, subject to the projection of p_i onto

s_j falling within the segment bounds. If the projection falls outside, the distance to the nearest endpoint is used:

$$d(p_i, s_j) = \begin{cases} d_{\perp}(p_i, s_j), & \text{if } \lambda^* \in [0, 1] \\ \min(\|p_i - \mathbf{a}_j\|, \|p_i - \mathbf{b}_j\|), & \text{otherwise} \end{cases} \quad (24)$$

where $\lambda^* = \frac{(p_i - \mathbf{a}_j) \cdot \vec{v}_j}{\|\vec{v}_j\|^2}$ is the normalized position of the orthogonal projection.

This yields a set of distances $\mathcal{D} = \{d_i\}_{i=1}^N$ for N trajectory points. Because all distances are non-negative by construction, their distribution approximates a half-normal form. To enable the use of established parametric inference, we mirror the data to create a synthetic sample:

$$\mathcal{D}_{\text{sym}} = \{d_i\}_{i=1}^N \cup \{-d_i\}_{i=1}^N \quad (25)$$

We fit a normal distribution to \mathcal{D}_{sym} using maximum likelihood estimation (MLE):

$$(\hat{\mu}, \hat{\sigma}) = \arg \max_{\mu, \sigma} \prod_{i=1}^{2N} \frac{1}{\sigma \sqrt{2\pi}} \exp\left(-\frac{(d_i - \mu)^2}{2\sigma^2}\right) \quad (26)$$

The rationale for using a normal model lies in its statistical tractability, allowing concise parameterization of alignment dispersion. The std $\hat{\sigma}$ serves as the principal indicator of horizontal alignment quality; lower values indicate that most trajectory points are concentrated near the centerline, reflecting more accurate registration. The mean $\hat{\mu}$ quantifies the average offset. To identify local misalignments, we define an outlier threshold as $\tau = \hat{\mu} + 2\hat{\sigma}$, classifying any $d_i > \tau$ as a significant deviation.

2) *Intersection Offset Evaluation*: For evaluation of structural alignment, we extract intersection centroids from both the registered point cloud and the reference map. Let $\mathcal{P}_I = \{p_i\}$ and $\mathcal{M}_I = \{m_i\}$ denote the sets of corresponding intersection centers in point cloud and map, respectively, with one-to-one correspondence established via nearest-neighbor search within a radius δ .

The mean intersection offset is computed as:

$$E_{\text{int}} = \frac{1}{K} \sum_{i=1}^K \|p_i - m_i\|_2 \quad (27)$$

where $K = |\mathcal{P}_I|$ is the number of matched intersection pairs. This metric reflects the degree to which salient topological features are spatially coincident after registration. The use of intersections, which are stable and easily distinguishable across representations, reduces sensitivity to local ambiguities and supports robust comparison even in the absence of GNSS or dense ground truth.

IV. EXPERIMENTS

This section presents a detailed experimental evaluation of the proposed geo-registration and spatial correction framework on two large-scale urban datasets under both GNSS-available and GNSS-denied conditions. We first describe the characteristics and acquisition procedures of the KITTI and Perth CBD LiDAR datasets, which provide diverse urban scenes and varying sensor modalities. We then outline the

experimental setup, including hardware configuration, software environment, and algorithmic parameters. Quantitative and qualitative results are reported for both planimetric (XY plane) and elevation (Z axis) alignment tasks. Metrics such as centerline distance error, elevation error, and correlation with ground-truth reference data are used to assess the performance improvements achieved by the framework. Through these experiments, we demonstrate the effectiveness, robustness, and generalizability of the proposed method across different urban scenarios and mapping challenges.

A. Dataset Description

To comprehensively evaluate the proposed urban LiDAR point cloud geo-registration with spatial correction framework, we conducted experiments on two representative large-scale datasets: the KITTI dataset and a high-definition LiDAR map of the Perth CBD. These datasets provide diverse urban scenes and varying sensor conditions, supporting rigorous testing of geo-registration and spatial correction performance in both GNSS-available and GNSS-denied scenarios.

1) *KITTI Dataset*: The KITTI dataset is widely recognized in the autonomous driving research community and is collected in Karlsruhe, Germany [59]. The dataset includes synchronized data streams from a Velodyne HDL-64E LiDAR sensor, high-resolution stereo cameras, and an integrated GPS/IMU navigation system. The LiDAR sensor provides 3D point clouds at 10 Hz, with each scan containing up to 130,000 points and a 360° horizontal field of view. The GPS/IMU subsystem enables centimeter-level pose annotation for each frame, supporting ground truth evaluation. For our experiments, we selected sequences 00, 02, 05, 08, and 09, which collectively cover a variety of urban settings including downtown areas, residential neighborhoods, and suburban roadways. These sequences exhibit complex road network geometries and include challenges such as occlusions, dynamic objects, and varying road surfaces. Each sequence consists of several thousand consecutive frames, with the associated GNSS information. The KITTI dataset's precise sensor calibration and comprehensive scene diversity make it an established benchmark for validating urban-scale point cloud alignment and spatial correction algorithms.

2) *Perth CBD LiDAR Map 2021*: The Perth CBD dataset [60] is a high-resolution 3D LiDAR map collected by our research team, covering the Perth CBD, Australia. Data acquisition was performed using a vehicle-mounted Ouster OS1-64 digital LiDAR sensor, offering 64 vertical channels and up to 2048 horizontal scan resolution. The sensor was mounted 1.5 m above ground level and operated at 10 frames per second during data capture. The data collection spanned three two-hour sessions, covering all major traffic routes in a closed-loop fashion to minimize drift and maximize map coverage. The resulting dataset comprises approximately 150,000 frames, totaling over 64 million points and encompassing a ground area of approximately 3 km × 1.2 km (nearly 4 km²). To ensure map quality, closed spatial loops were extracted from the raw LiDAR stream using an automatic loop detection algorithm based on registration RMSE, and all frames within each loop

were sequentially aligned using a 3D Normal Distributions Transform (NDT) algorithm. The final map contains binary annotation separating ground (road) points from non-ground objects such as buildings, vegetation, and street furniture. Notably, the Perth CBD dataset does not contain GNSS or GPS/IMU information, making it an ideal testbed for geo-registration methods operating under GNSS-denied conditions. Road intersection positions and topological features are used as ground truth references for evaluating alignment accuracy.

3) *Reference Map and Elevation Data*: For both datasets, 2D reference maps were sourced from the Google Maps API at zoom level 18, with Mercator projection ensuring accurate spatial reference. At the Perth CBD latitude (-31°), the map resolution is 0.512 meters per pixel; at the KITTI location in Karlsruhe (49°), the resolution is 0.392 meters per pixel. To enable vertical alignment, we incorporated elevation information from the SRTM 30m Global 1 arc second V003 dataset (NASA/NGA)[61], which provides global digital elevation models with a spatial resolution of 30 meters and vertical root mean square error (RMSE) of ± 3.56 meters. This dataset covers both the Perth and Karlsruhe regions and ensures that our spatial correction procedure addresses both horizontal and vertical registration errors.

B. Experimental Setup

All experiments were performed on a workstation equipped with an Intel Core i9-10900K CPU (10 cores, 3.7 GHz), 32 GB DDR4 memory, and an NVIDIA GeForce RTX 3080 GPU (12 GB VRAM), running Microsoft Windows 10 Professional. The system included a 1 TB NVMe SSD to support efficient access and processing of large-scale LiDAR datasets.

The experimental pipeline was implemented in Python 3.9 using Anaconda for environment management. Core libraries included NumPy, SciPy, Open3D, scikit-learn, Matplotlib, and OpenCV 4.5. Deep learning inference for semantic segmentation was based on PyTorch 1.13 with CUDA 11.6 support. Key algorithm parameters were empirically set: keypoint matching threshold at 8 pixels, skeleton extraction density at 40, RBF interpolation parameter $\epsilon = 5$, and correspondence distance threshold at 30 pixels. Point cloud preprocessing used 20 nearest neighbors and a Std multiplier of 2.0 for outlier removal. All code, data processing, and visualization steps were performed under controlled and reproducible conditions.

C. Results on the KITTI Dataset

This section presents a comprehensive evaluation of the proposed geo-registration and spatial correction framework on the KITTI dataset. We report both planimetric (XY plane) and elevation (Z axis) alignment results across five representative urban driving sequences, quantitatively analyzing the reduction in alignment error before and after applying our method. The results include std and mean error metrics, empirical error distribution plots, and qualitative visualizations of trajectory-to-map correspondence. Through these analyses, we demonstrate the effectiveness of the proposed approach in mitigating global and local spatial misalignments, ensuring precise 3D map consistency even under diverse urban conditions and varying initial sensor errors.

1) *Planimetric (XY) Alignment Performance on KITTI Dataset*: We applied the proposed geo-registration with spatial correction framework to five urban sequences from the KITTI dataset (00, 02, 05, 08, 09) to evaluate performance across diverse urban scenarios.

The upper portion of Figure 2 illustrates the overall alignment between the LiDAR trajectory and the urban road network for the selected KITTI sequences (00, 02, 05, 08, and 09). The registered point cloud trajectories (magenta) are superimposed on reference map backgrounds. The visualizations confirm that the registered trajectories follow the underlying urban road network structure with high fidelity, including intersections, curves, and closed loops, without requiring GNSS-based initialization.

Figure 3 provides frame-level local alignment results for representative samples in each KITTI sequence. For each frame, the green dot indicates the estimated position after geo-registration, the blue dot represents manually labeled ground truth, and the yellow dot marks the GPS annotation provided in KITTI. The red overlay shows the LiDAR point cloud projected onto the map. The visual consistency between green and blue dots in various urban and residential scenes demonstrates the accuracy of the proposed method, with the estimated positions closely matching ground truth and outperforming raw GPS labels in several challenging cases.

While the visual results qualitatively demonstrate the outcome of the alignment, we further conducted a quantitative evaluation to assess planimetric accuracy across these selected KITTI sequences. Specifically, we measured the Euclidean distance between the registered LiDAR trajectory and the corresponding road centerline extracted from the reference map, which serves as the principal metric for assessing spatial alignment.

Table I summarizes the planimetric alignment results across five KITTI sequences, reporting the std and mean error of the centerline distance both before and after spatial correction. For comparison, statistics from the raw KITTI GPS data are also included. The results demonstrate that the proposed pipeline significantly improves spatial alignment, reducing the average std from 3.25 m to 0.84 m and the mean error from 2.60 m to 0.69 m. Notably, in all five sequences, the final planimetric accuracy surpasses that of the original GPS-based annotations, with both metrics consistently outperforming the KITTI GNSS reference (average std 1.88 m, mean 1.38 m). Among the sequences, Sequence 05 achieves the lowest post-correction deviation (std 0.57 m), likely due to its regular road layout and well-defined intersections. Sequence 08, which exhibits the largest initial misalignment (std 5.21 m), shows substantial improvement (std 1.35 m) despite the complexity of its road topology.

The improvements are visually substantiated by the point pair distance distribution plots shown in Figure 4. Each plot compares the empirical distribution of point-to-centerline distances for three cases: the raw GPS reference, the initial (rigid) alignment, and the final (non-rigid) registration. After the proposed spatial correction, the distributions become sharply peaked and shift toward lower error values, matching the spread of the KITTI GNSS reference or outperforming it in

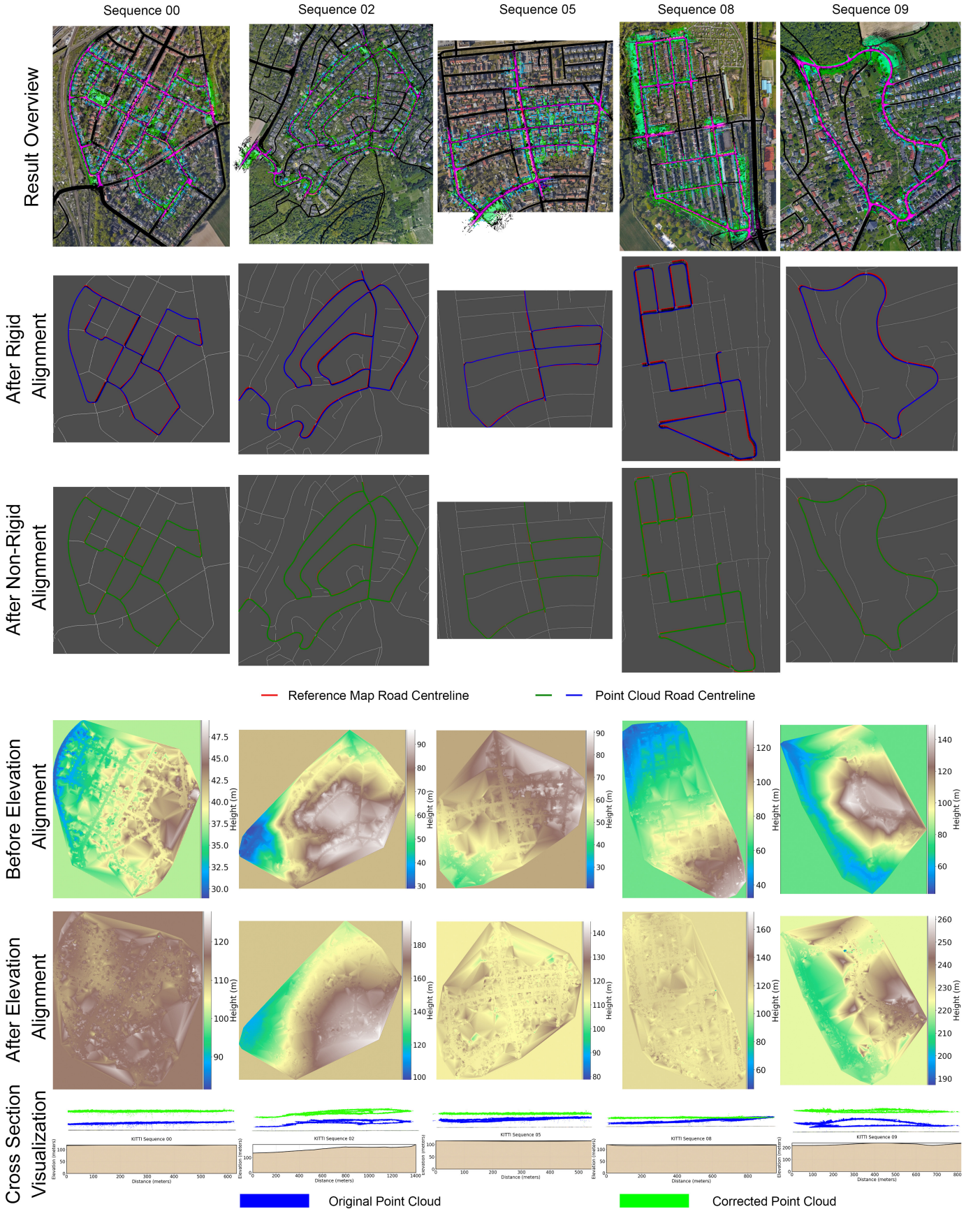


Fig. 2. Overall alignment results for selected KITTI sequences (00, 02, 05, 08, 09). Magenta curves show the geo-registered point cloud trajectories overlaid on reference map tiles, demonstrating close correspondence with the urban road network across diverse scenarios.



Fig. 3. Frame-level registration results for selected frames in each KITTI sequence. Green dots: estimated trajectory points after geo-registration. Blue dots: manually labeled ground truth. Yellow dots: GPS-based reference. LiDAR points (red) are projected on the underlying map imagery. The results confirm accurate local alignment under diverse urban conditions.

TABLE I
KITTI DATASET PLANIMETRIC ALIGNMENT ACCURACY (XY PLANE)

Sequence	Centerline Distance std Before Correction (m)	Centerline Distance std After Correction (m)	KITTI GPS Distance std (m)	Centerline Distance Mean Error Before Correction (m)	Centerline Distance Mean Error After Correction (m)	KITTI GPS Distance Mean (m)
00	2.60	0.76	1.22	2.11	0.63	0.89
02	3.42	0.88	1.45	2.49	0.77	1.03
05	2.10	0.57	1.45	1.66	0.45	1.13
08	5.21	1.35	2.95	4.26	1.08	2.14
09	2.90	0.64	2.35	2.48	0.53	1.72
Avg	3.25	0.84	1.88	2.60	0.69	1.38

TABLE II
KITTI DATASET ELEVATION ALIGNMENT ACCURACY (Z AXIS)

Sequence	Elevation Distance std Before (m) ↓	Elevation Distance std After (m) ↓	Mean Error Before (m) ↓	Mean Error After (m) ↓	Elevation Correlation (r.) Before ↑	Elevation Correlation (r.) After ↑
00	1.70	0.95	1.42	0.59	0.29	0.69
02	12.96	5.76	11.76	4.49	0.94	0.96
05	0.72	1.19	0.56	0.83	0.77	0.62
08	6.84	1.92	3.10	1.16	0.11	0.62
09	9.35	4.41	6.77	3.59	0.85	0.94
Average	6.31	2.85	4.72	2.13	0.59	0.77

some frames. For example, in Sequence 00 as shown in the top-left subplot of Fig. 4, the post-correction std (0.76 m) closely matches the GPS reference (1.22 m), and the heavy-tailed error seen in the rigid alignment is substantially suppressed. Across all sequences, the number of outlier points at large distances is reduced after non-rigid alignment, indicating not only the reduction of global drift but also the mitigation of local deformation. The error histograms demonstrate that the final results achieve a high degree of geometric consistency with the map reference, robust to variations in scene topology, occlusion, or dynamic interference present in the urban environment.

2) *Elevation (Z Axis) Alignment Performance on KITTI Dataset:* Beyond planar alignment, we quantitatively assessed the effectiveness of the proposed framework in correcting vertical (elevation) deviations between LiDAR point clouds and the map-based elevation references. The lower portion of Figure 2 demonstrates the visual results of elevation alignment, where our correction method shows clear improvements compared to the original KITTI data. This improvement is evident in both the height map color representation and the cross-section comparison plots at the bottom of the figure. The corrected point clouds exhibit better vertical consistency and reduced elevation artifacts, as visualized through the color-coded height maps and the elevation profile comparisons.

Figure 5 provides a comprehensive analysis of the elevation alignment results for the five evaluated KITTI sequences, with each row corresponding to a distinct sequence. In each group, the left subplot presents a scatter plot comparing measured elevation values from the LiDAR point cloud (green) and the corresponding ground-truth terrain map elevation for each spatial location. The correlation coefficients (r) for both the raw KITTI GPS data and the proposed method after correction are reported directly on each plot, serving as quantitative indicators of vertical alignment quality. For example, in Sequence 00, the initial GPS data yields a correlation coefficient of 0.289, whereas the corrected point cloud achieves 0.691, reflecting a substantial improvement in vertical consistency. Similarly, for Sequence 02 and Sequence 09, the correlation values rise from 0.936 to 0.963 and from 0.846 to 0.936, respectively, after correction, indicating that the proposed method brings the point cloud elevation into much closer agreement with the terrain reference. In contrast, Sequence 08, which initially has a very weak correlation ($r = 0.112$), sees a marked enhancement ($r = 0.618$) following correction, demonstrating the robustness of the method even in

challenging cases with significant elevation drift. The right subplot in each group illustrates the empirical distribution of elevation errors—computed as the difference between the measured point cloud elevations and the corresponding terrain map values—for both the GPS-based and the corrected results. The histograms visualize the density and spread of elevation errors before and after spatial correction, while the overlaid curves represent fitted distributions with reported std values. Across all sequences, the GPS-based results exhibit broader, heavy-tailed distributions with large standard deviations, indicating substantial vertical deviation from the terrain ground truth. After correction, the error distributions of the point cloud results become much narrower and more sharply peaked around zero, with a pronounced reduction in std. For instance, in Sequence 02, the std is reduced from 12.96 m (GPS) to 5.76 m (corrected), and in Sequence 09, from 9.35 m to 4.41 m, respectively. The concentration of errors near zero demonstrates that the proposed framework is effective in mitigating both systematic elevation offsets and local inconsistencies, thereby restoring the vertical geometric integrity of the 3D urban map.

Taken together, these visualizations and metrics confirm that the proposed elevation correction strategy consistently improves the vertical alignment of LiDAR point clouds with respect to reference terrain models. The improvements are robust across various urban topologies, initial error levels, and scene complexities. This enhanced elevation accuracy is crucial for downstream applications such as high-definition map generation, 3D city modeling, infrastructure assessment, and sensor fusion, where precise vertical consistency with geospatial references is required.

D. Results on the Perth CBD Dataset

To further validate the robustness and scalability of the proposed geo-registration and spatial correction framework in GNSS-denied scenarios, we conducted experiments on the Perth CBD dataset.

Figure 6 presents comprehensive qualitative results. The top row displays the overall point cloud overlay for three representative closed-loop regions (Perth CBD-01, -02, -03) and the complete map. The color-coded elevation indicates height variations across the urban environment, while the superimposed trajectories demonstrate that the corrected point cloud maintains consistent alignment with the underlying road network, including sharp curves, intersections, and block structures. This global map-level consistency is achieved solely

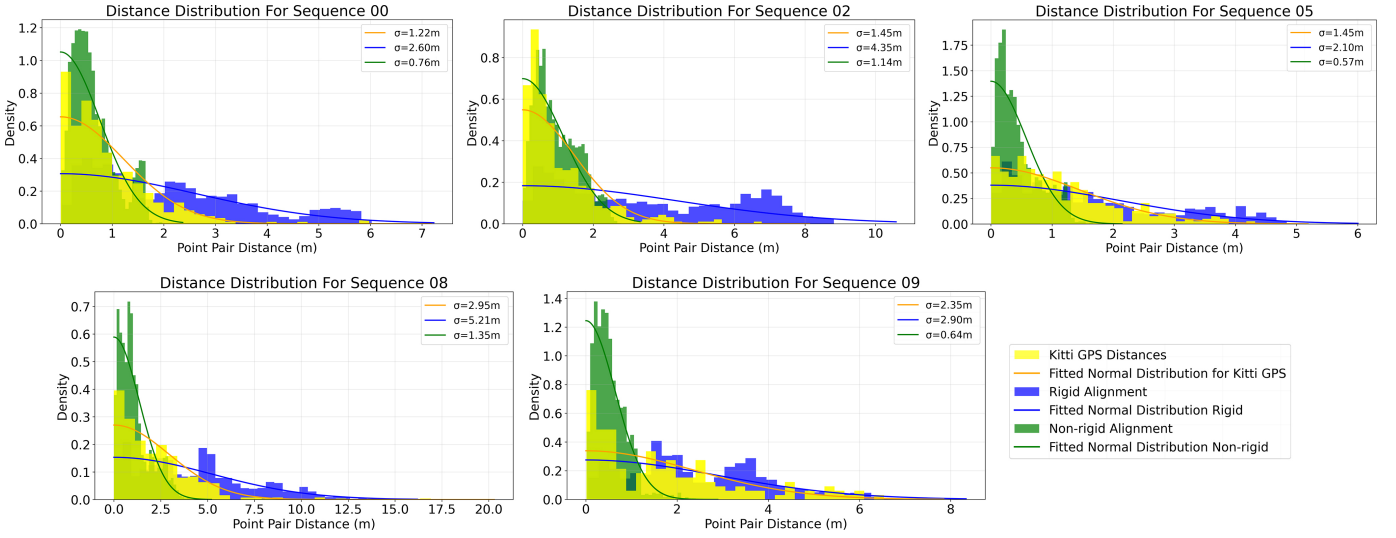


Fig. 4. Point-pair distance distribution analysis across five KITTI sequences. Histograms compare distance measurements between KITTI GPS data (yellow) and our point cloud method using rigid alignment (blue) and non-rigid alignment (green), with overlaid fitted normal distributions and std (σ) for each approach.

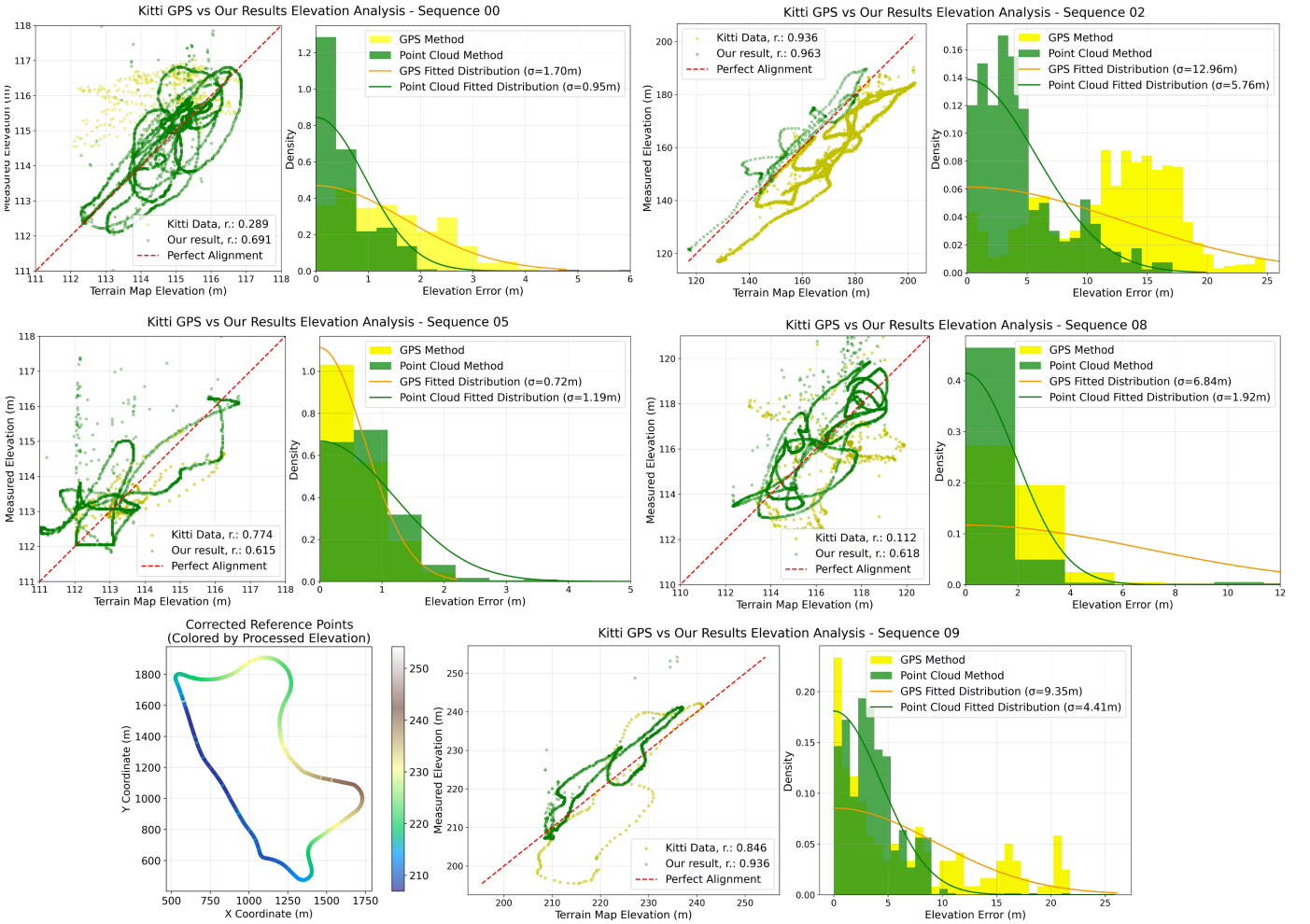


Fig. 5. Cross-sequence validation of elevation correction accuracy. Comparison of KITTI GPS data and our point cloud method across sequences 00, 02, 05, 08, and 09. The left plot shows point index-based correlation plots of corrected elevations against ground truth elevation data, while the right plot displays error probability distributions with std values of fitted distributions (σ) for each approach. The bottom left subfigure shows the XY-plane visualization of the corrected elevations for sequence 09.

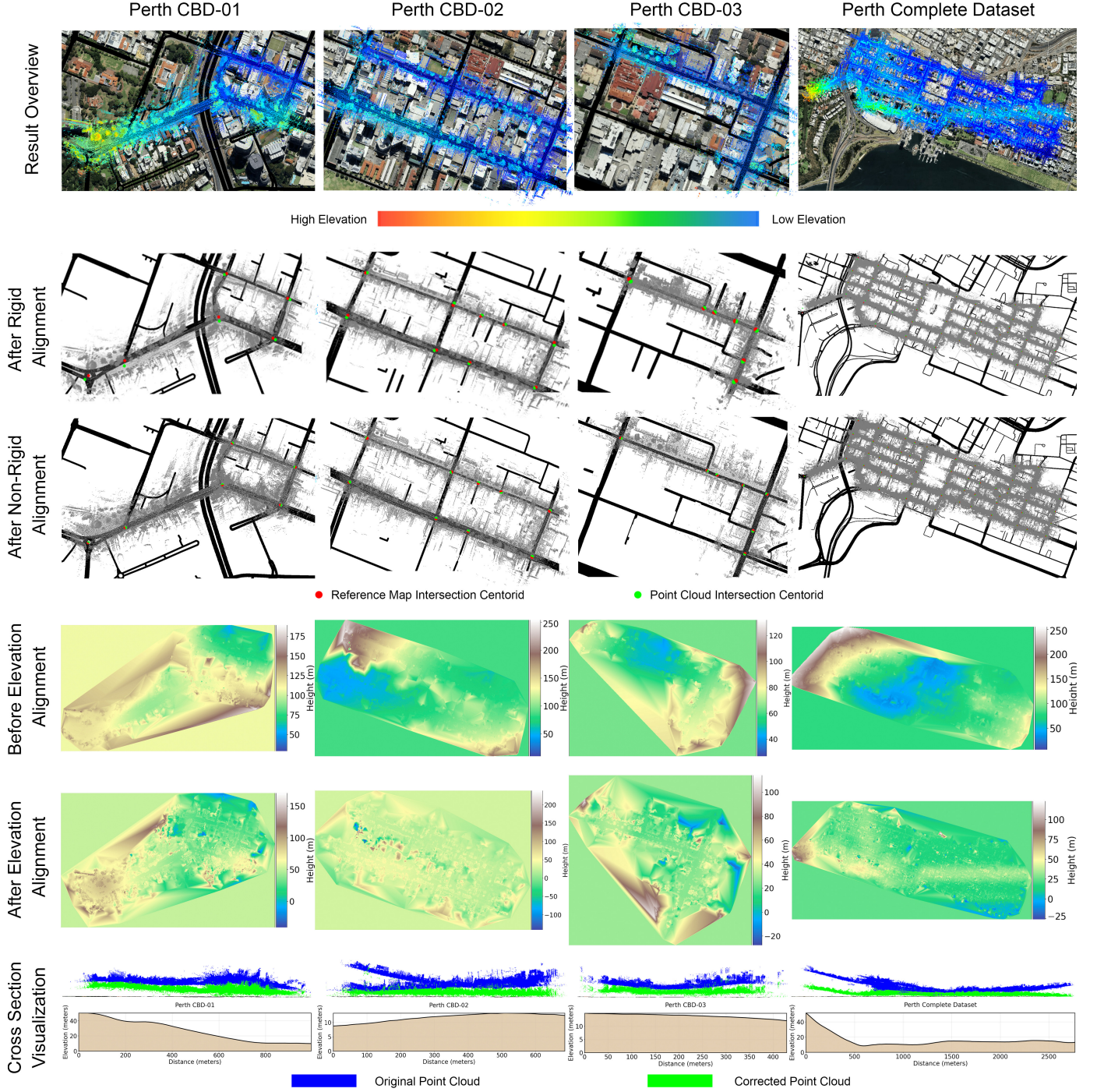


Fig. 6. Qualitative results for the Perth CBD dataset. Top: point cloud alignment and map overlay for three closed loops and the complete map. Middle: comparison of intersection centroid positions before/after correction (red: map, green: point cloud). Bottom: elevation alignment results, including before/after alignment maps and cross-section profiles, showing significant reduction in global and local elevation discrepancies.

TABLE III
PERTH CBD DATASET PLANIMETRIC ALIGNMENT ACCURACY (XY PLANE)

Sequence	Point Pair Distance std Before Non-Rigid Transform (m)	Point Pair Distance std After Non-Rigid Transform (m)	Point Pair Distance Mean Before Non-Rigid Transform (m)	Point Pair Distance Mean After Non-Rigid Transform (m)
Perth-01	4.34	0.95	7.32	0.87
Perth-02	3.19	0.93	3.03	0.83
Perth-03	2.18	0.89	1.97	0.84
Perth Complete	7.27	1.07	5.09	2.17
Average	4.24	0.96	4.35	1.18

TABLE IV
PERTH DATASET ELEVATION ALIGNMENT ACCURACY (Z AXIS)

Sequence	Elevation Distance std Before (m) ↓	Elevation Distance std After (m) ↓	Mean Error Before (m) ↓	Mean Error After (m) ↓	Elevation Correlation (r.) Before ↑	Elevation Correlation (r.) After ↑
CBD-01	3.15	0.82	2.89	1.45	0.76	0.94
CBD-02	20.15	2.12	17.84	3.03	0.22	0.81
CBD-03	9.95	1.64	8.67	1.32	0.65	0.84
Complete	18.23	4.88	15.35	3.91	0.38	0.86
Average	12.87	3.37	11.19	2.73	0.52	0.78

through map and intersection-based correction, without relying on external positioning sensors.

The middle section of Figure 6 compares intersection centroid alignment before and after the non-rigid spatial correction. Red points represent intersection centroids extracted from the 2D map, and green points denote corresponding centroids detected in the LiDAR-derived road skeleton. Before correction, significant global drift and local misalignments can be observed, especially in the periphery of each subregion and in dense road network clusters. After applying the full framework, the majority of green points closely coincide with the red reference, indicating that the framework is effective in reducing both large-scale displacement and small-scale geometric errors. This is critical for city-scale applications, where intersection accuracy impacts traffic simulation, network analysis, and downstream urban analytics.

Table III quantitatively summarizes the improvements in planimetric (XY) alignment for all evaluated regions. The std of point pair distances (intersection centroid-to-centroid error) decreases from an average of 4.24 m before correction to 0.96 m after applying the non-rigid transformation. Similarly, the mean error is reduced from 4.35 m to 1.18 m. Subregion CBD-01 achieves the lowest post-correction std of 0.95 m, reflecting the regular grid layout and dense intersection structure, while the full dataset, covering all loops, maintains high accuracy (std 1.07 m) despite complex road geometries and network density. These results indicate the method’s effectiveness in addressing both local misalignment and cumulative global drift in large-scale, real-world city mapping.

The lower part of Figure 6 visualizes the effect of elevation alignment. For each region, we provide elevation raster maps before and after correction, as well as cross-sectional height profiles along representative road segments. Prior to correction, the LiDAR point cloud exhibits both global elevation bias and local inconsistency, manifested as undulating surfaces and discontinuities when compared to terrain references. After correction, these discrepancies are substantially mitigated. The elevation profiles demonstrate that the point cloud aligns with the ground truth terrain and remains continuous across the mapped area, confirming the removal of accumulated vertical drift and the restoration of geometric integrity required for further semantic mapping and 3D city modeling.

To complement the visual assessment, Table IV provides quantitative evaluation of elevation alignment accuracy across all subregions. The elevation std decreased from an average of 12.87 m before correction to 3.37 m after correction, and the mean elevation error dropped from 11.19 m to 2.73 m.

Elevation correlation improved markedly, from 0.52 to 0.78 on average, indicating a substantially closer fit between the corrected LiDAR elevations and the terrain reference. Among all subregions, CBD-02 exhibited the largest improvement, with the std reduced from 20.15 m to 2.12 m and correlation increasing from 0.22 to 0.81. These results validate the effectiveness of the proposed terrain-aware elevation correction in mitigating both large-scale vertical drift and local inconsistencies across complex city-scale datasets.

V. CONCLUSION

In this work, we addressed the challenge of accurate geo-registration for urban LiDAR point clouds in scenarios with limited or unavailable GNSS information, particularly in dense urban environments. The proposed framework integrates semantic segmentation, topology-based skeleton extraction, and a hierarchical spatial correction pipeline that combines global rigid alignment with non-rigid radial basis function (RBF) interpolation and terrain-aware elevation adjustment. Experimental results on both the KITTI and Perth CBD datasets demonstrate that the method effectively reduces alignment errors in both planimetric and elevation dimensions. Specifically, the standard deviation of road centerline distance on the KITTI dataset decreased from 3.25 m to 0.84 m, with the mean error reduced from 2.60 m to 0.69 m. On the Perth CBD dataset, the standard deviation dropped from 4.24 m to 0.96 m, and the mean error from 4.35 m to 1.18 m, based on intersection centroids. In the elevation dimension, our method achieved reductions of 3.46 m and 9.50 m in elevation standard deviation on the KITTI and Perth datasets, respectively, while elevation correlation improved by 0.18 and 0.26. These results confirm that the proposed method effectively aligns input point cloud data with satellite maps to recover precise GNSS information, outperforming traditional registration approaches in both global and local alignment. This enables high-precision 3D urban mapping in GNSS-denied settings.

Future work will focus on extending the framework for full-scale city-wide deployment, incorporating dynamic urban features, and improving robustness to occlusions, structural inconsistencies, and incomplete map data, with the goal of supporting real-world localization and autonomous system applications in complex urban environments.

REFERENCES

- [1] Philipp R.W. Urech, Maria Angela Dissegna, Christophe Girot, and Adrienne Grêt-Regamey. Point cloud modeling as a bridge between landscape design and planning. *Landscape and Urban Planning*, 203:103903, 2020.

- [2] Nico Cornelis, Bastian Leibe, Kurt Cornelis, and Luc Van Gool. 3d urban scene modeling integrating recognition and reconstruction. *International Journal of Computer Vision*, 78:121–141, 07 2008.
- [3] Gilles-Antoine Nys, Florent Poux, and Roland Billen. Cityjson building generation from airborne lidar 3d point clouds. *ISPRS International Journal of Geo-Information*, 9(9), 2020.
- [4] Qingyong Hu, Bo Yang, Sheikh Khalid, Wen Xiao, Niki Trigoni, and Andrew Markham. Towards semantic segmentation of urban-scale 3d point clouds: A dataset, benchmarks and challenges. In *Proceedings of the IEEE/CVF Conference on Computer Vision and Pattern Recognition*, 2021.
- [5] Xixun Wang, Yoshiki Mizukami, Makoto Tada, and Fumitoshi Matsuno. Navigation of a mobile robot in a dynamic environment using a point cloud map. *Artificial Life and Robotics*, 26:10–20, 2021.
- [6] Zhicheng Zhou, Cheng Zhao, Daniel Adolfsson, Songzhi Su, Yang Gao, Tom Duckett, and Li Sun. Ndt-transformer: Large-scale 3d point cloud localisation using the normal distribution transform representation. In *2021 IEEE international conference on robotics and automation (ICRA)*, pages 5654–5660. IEEE, 2021.
- [7] Martin Mokroš, Tomáš Mikita, Arunima Singh, Julián Tomaščík, Juliána Chudá, Piotr Weżyk, Karel Kuželka, Peter Surový, Martin Klimánek, Karolína Zięba-Kulawik, Rogério Bobrowski, and Xinlian Liang. Novel low-cost mobile mapping systems for forest inventories as terrestrial laser scanning alternatives. *International Journal of Applied Earth Observation and Geoinformation*, 104:102512, 2021.
- [8] Liang Cheng, Yang Wu, Yu Wang, Lishan Zhong, Yanming Chen, and Manchun Li. Three-dimensional reconstruction of large multilayer interchange bridge using airborne lidar data. *IEEE Journal of Selected Topics in Applied Earth Observations and Remote Sensing*, 8(2):691–708, 2015.
- [9] Yirui Zhang, Jiabo Xu, Yanni Zou, Peter X. Liu, and Jie Liu. Ps-net: Point shift network for 3-d point cloud completion. *IEEE Transactions on Geoscience and Remote Sensing*, 60:1–13, 2022.
- [10] Xinlian Liang, Yunsheng Wang, Anttoni Jaakkola, Antero Kukko, Harri Kaartinen, Juha Hyyppä, Eija Honkavaara, and Jingbin Liu. Forest data collection using terrestrial image-based point clouds from a handheld camera compared to terrestrial and personal laser scanning. *IEEE Transactions on Geoscience and Remote Sensing*, 53(9):5117–5132, 2015.
- [11] Letian Gao, Xin Xia, Zhaoliang Zheng, and Jiaqi Ma. Gnnslidar fusion for vehicle localization in urban driving environments within a consensus framework. *Mechanical Systems and Signal Processing*, 205:110862, 2023.
- [12] Shuting Zhang, Hongtao Wang, Cheng Wang, Yingchen Wang, Shaohui Wang, and Zhenqi Yang. An improved ransac-icp method for registration of slam and uav-lidar point cloud at plot scale. *Forests*, 15(6):893, 2024.
- [13] Kenji Koide, Masashi Yokozuka, Shuji Oishi, and Atsuhiko Banno. Voxelized gicp for fast and accurate 3d point cloud registration. In *2021 IEEE International Conference on Robotics and Automation (ICRA)*, pages 11054–11059. IEEE, 2021.
- [14] Leping He, Shuaiqing Wang, Qijun Hu, Qijie Cai, Muyao Li, Yu Bai, Kai Wu, and Bo Xiang. Gfoicp: Geometric feature optimized iterative closest point for 3-d point cloud registration. *IEEE Transactions on Geoscience and Remote Sensing*, 61:1–17, 2023.
- [15] Han Wang, Chen Wang, Chun-Lin Chen, and Lihua Xie. F-loam : Fast lidar odometry and mapping. In *2021 IEEE/RSJ International Conference on Intelligent Robots and Systems (IROS)*, page 4390–4396. IEEE Press, 2021.
- [16] Hongliang Guo, Jiankang Zhu, and Yunping Chen. E-loam: Lidar odometry and mapping with expanded local structural information. *IEEE transactions on intelligent vehicles*, 8(2):1911–1921, 2022.
- [17] Martin Oelsch, Mojtaba Karimi, and Eckehard Steinbach. R-loam: Improving lidar odometry and mapping with point-to-mesh features of a known 3d reference object. *IEEE Robotics and Automation Letters*, 6(2):2068–2075, 2021.
- [18] Jianping Li, Weitong Wu, Bisheng Yang, Xianghong Zou, Yandi Yang, Xin Zhao, and Zhen Dong. Whu-helmet: A helmet-based multisensor slam dataset for the evaluation of real-time 3-d mapping in large-scale gnss-denied environments. *IEEE Transactions on Geoscience and Remote Sensing*, 61:1–16, 2023.
- [19] Yuhang Xu, Chi Chen, Bisheng Yang, Weitong Wu, Shangzhe Sun, Zhiye Wang, Liuchun Li, and Qin Zou. Atcm: Aerial-terrestrial lidar-based collaborative simultaneous localization and mapping. *IEEE Transactions on Geoscience and Remote Sensing*, 63:1–14, 2025.
- [20] Pei Sun, Henrik Kretschmar, Xerxes Dotiwalla, Aurelien Chouard, Vijaysai Patnaik, Paul Tsui, James Guo, Yin Zhou, Ying Chai, Benjamin Caine, Vasanth Vasudevan, Wei Han, Jiquan Ngiam, Brian Sapp, Sami Omari, Shuyang An, Yuning Mao, and Raquel Urtasun. Scalability in perception for autonomous driving: Waymo open dataset. *Proceedings of the IEEE/CVF Conference on Computer Vision and Pattern Recognition (CVPR)*, pages 2446–2454, 2020.
- [21] Muhammad Ibrahim, Naveed Akhtar, Mohammad A. A. K. Jalwana, Michael Wise, and Ajmal Mian. High definition lidar mapping of perth cbd. In *2021 Digital Image Computing: Techniques and Applications (DICTA)*, pages 01–08, 2021.
- [22] Muhammad Ibrahim, Naveed Akhtar, Saeed Anwar, and Ajmal Mian. Swan 3d point cloud dataset, 2023.
- [23] Chanachon Pajitrapaporn, Thayathip Thongtan, and Chalermchon Satriapod. Accuracy assessment of integrated gnss measurements with lidar mobile mapping data in urban environments. *Measurement: Sensors*, 18:100078, 2021.
- [24] Paul D. Groves, Ziyi Jiang, Lei Wang, and Marek K. Ziebart. Shadow matching: A new gnss positioning technique for urban canyons. *The Journal of Navigation*, 65(3):417–430, 2011.
- [25] Chen Wang, Shiyu Mao, Ben M. Chen, and Tomas Moore. Safe path planning for uav urban operation under gnss signal occlusion risk. *Robotics and Autonomous Systems*, 142:103800, 2021.
- [26] Ioannis Antonopoulos, Valentin Robu, Benoit Couraud, Desen Kirli, Sonam Norbu, Aristides Kiprakis, David Flynn, Sergio Elizondo-Gonzalez, and Stephen Wattam. Sensor data quality: a systematic review. *Journal of Big Data*, 7(1):1–49, 2020.
- [27] Julius Degeys, Ian Rose, Ankit Patel, and Radhika Nagpal. Desync: self-organizing desynchronization and tdma on wireless sensor networks. In *Proceedings of the 6th international conference on Information processing in sensor networks*, pages 11–20. IEEE, 2007.
- [28] Wenbo Zhang, Hongwei Li, Jian Wang, and Xiaolong Chen. Radar point cloud synchronization and simulation method under multi-condition constraints. In *2023 IEEE Intelligent Vehicles Symposium (IV)*, pages 1–6. IEEE, 2023.
- [29] Weisong Wen, Yiyang Zhou, Guohao Zhang, Saman Fahandezh-Saadi, Xiwei Bai, Wei Zhan, Masayoshi Tomizuka, and Li-Ta Hsu. Urbanloco: A full sensor suite dataset for mapping and localization in urban scenes. In *2020 IEEE International Conference on Robotics and Automation (ICRA)*, pages 2310–2316, 2020.
- [30] Martin Weinmann, Boris Jutzi, and Clément Mallet. Georeferenced point clouds: A survey of features and point cloud management. *ISPRS International Journal of Geo-Information*, 2(4):1038–1065, 2013.
- [31] Charlotte Leigh, David Kidner, and Malcolm Thomas. The use of lidar in digital surface modelling: Issues and errors. *T. GIS*, 13:345–361, 08 2009.
- [32] Yusheng Wang, Qing Chen, Qing Zhu, Linfu Liu, Chaokui Li, and Dehai Zheng. Multi-source point cloud registration for urban areas using a coarse-to-fine approach. *GIScience & Remote Sensing*, 61(1):2341557, 2024.
- [33] Paul D. Groves and Ziyi Jiang. Accurate georegistration of point clouds using geographic data. In *Proceedings of the 3DV 2014 - Second International Conference on 3D Vision*, pages 158–165. IEEE, 2014.
- [34] Peyman Azari, Songnian Li, Ahmed Shaker, and Shahram Sattar. Georeferencing building information models for bim/gis integration: A review of methods and tools. *ISPRS International Journal of Geo-Information*, 14(5), 2025.
- [35] Pengcheng Tang, Daniel Huber, Burcu Akinci, Robert Lipman, and Alan Lytle. Point cloud registration and change detection in urban environment using an onboard lidar sensor and mls reference data. *ISPRS Journal of Photogrammetry and Remote Sensing*, 187:119–136, 2022.
- [36] Cihan Altuntas. Georeferencing and reprojection error investigation on image based 3d digitization and mapping of historical buildings. *ISPRS - International Archives of the Photogrammetry, Remote Sensing and Spatial Information Sciences*, XLII-2/W11:71–75, 05 2019.
- [37] Jingbin Liu, Yifan Liang, Dong Xu, · Gong, and Juha Hyyppä. A ubiquitous positioning solution of integrating gnss with lidar odometry and 3d map for autonomous driving in urban environments. *Journal of Geodesy*, 05 2023.
- [38] Mariella Dreissig, Dominik Scheuble, Florian Piewak, and Joschka Boedecker. Survey on lidar perception in adverse weather conditions. In *Survey on LiDAR Perception in Adverse Weather Conditions*, 05 2023.
- [39] Radu Bogdan Rusu and Steve Cousins. 3d is here: Point Cloud Library (PCL). In *IEEE International Conference on Robotics and Automation*, pages 1–4. IEEE, 2011.
- [40] X. Chen, B. Kohlmeyer, M. Stroila, N. Alwar, R. Wang, and J. Bach. Next generation map making: geo-referenced ground-level LIDAR point clouds for automatic retro-reflective road feature extraction. In *ACM*

SIGSPATIAL International Conference on Advances in Geographic Information Systems, pages 488–491. ACM, 2009.

- [41] Charles R Qi, Li Yi, Hao Su, and Leonidas J Guibas. Pointnet++: Deep hierarchical feature learning on point sets in a metric space. *arXiv preprint arXiv:1706.02413*, 2017.
- [42] Xiaoyang Wu, Li Jiang, Peng-Shuai Wang, Zhijian Liu, Xihui Liu, Yu Qiao, Wanli Ouyang, Tong He, and Hengshuang Zhao. Point transformer v3: Simpler, faster, stronger. In *CVPR*, 2024.
- [43] A. Boyko and T. Funkhouser. Extracting roads from dense point clouds in large scale urban environment. *ISPRS Journal of Photogrammetry and Remote Sensing*, 66(6):S2–S12, 2011.
- [44] Y. Yu, J. Li, H. Guan, F. Jia, and C. Wang. Learning hierarchical features for automated extraction of road markings from 3-D mobile LiDAR point clouds. *IEEE Journal of Selected Topics in Applied Earth Observations and Remote Sensing*, 8(2):709–726, 2015.
- [45] Y. Gao, X. Huang, F. Zhang, Z. Fu, and C. Yang. Automatic geo-referencing mobile laser scanning data to UAV images. In *International Archives of the Photogrammetry, Remote Sensing and Spatial Information Sciences*, volume 40, pages 41–46, 2015.
- [46] Andrew Qu. Adaptive bird’s eye view description for long-term mapping and loop closure in 3d point clouds. *Applied and Computational Engineering*, 73:77–93, 07 2024.
- [47] A. Schindler, G. Maier, and F. Janda. Generation of high precision digital maps using circular arc splines. In *IEEE Intelligent Vehicles Symposium*, pages 246–251. IEEE, 2012.
- [48] B. Wu, B. Yu, W. Yue, S. Shu, W. Tan, C. Hu, Y. Huang, J. Wu, and H. Liu. A voxel-based method for automated identification and morphological parameters estimation of individual street trees from mobile laser scanning data. *Remote Sensing*, 5(2):584–611, 2013.
- [49] F.L. Bookstein. Principal warps: Thin-plate splines and the decomposition of deformations. *IEEE Transactions on Pattern Analysis and Machine Intelligence*, 11(6):567–585, 1989.
- [50] X. Huang, L. Zhang, and P. Li. An adaptive method for registration of airborne LiDAR point clouds using local spatial features. *Remote Sensing*, 5(11):5957–5977, 2013.
- [51] M. Li, L. Nan, N. Smith, and P. Wonka. Reconstructing building mass models from UAV images. *Computers & Graphics*, 54:84–93, 2016.
- [52] J. Ma, J. Zhao, and A.L. Yuille. Non-rigid point set registration by preserving global and local structures. *IEEE Transactions on Image Processing*, 25(1):53–64, 2016.
- [53] Z. Dong, F. Liang, B. Yang, Y. Xu, Y. Zang, J. Li, Y. Wang, W. Dai, H. Fan, J. Hyppä, and U. Stilla. Registration of large-scale terrestrial laser scanner point clouds: A review and benchmark. *ISPRS Journal of Photogrammetry and Remote Sensing*, 163:327–342, 2020.
- [54] F. Pomerleau, F. Colas, and R. Siegwart. A review of point cloud registration algorithms for mobile robotics. *Foundations and Trends in Robotics*, 4(1):1–104, 2015.
- [55] Y. Yu, J. Li, H. Guan, C. Wang, and J. Yu. Semiautomated extraction of street light poles from mobile LiDAR point-clouds. *IEEE Transactions on Geoscience and Remote Sensing*, 53(3):1374–1386, 2014.
- [56] H. Wu, X. He, P. Gamba, and Z. Li. Massive urban point cloud registration through 2D-3D linear alignment. *ISPRS Journal of Photogrammetry and Remote Sensing*, 154:153–169, 2019.
- [57] Xiaoyang Wu, Yixing Lao, Li Jiang, Xihui Liu, and Hengshuang Zhao. Point transformer v2: Grouped vector attention and partition-based pooling. In *NeurIPS*, 2022.
- [58] Martin Ester, Hans-Peter Kriegel, Jörg Sander, and Xiaowei Xu. A density-based algorithm for discovering clusters in large spatial databases with noise. In *Proceedings of the Second International Conference on Knowledge Discovery and Data Mining, KDD’96*, page 226–231. AAAI Press, 1996.
- [59] Andreas Geiger, Philip Lenz, Christoph Stiller, and Raquel Urtasun. Vision meets robotics: The kitti dataset. *International Journal of Robotics Research (IJRR)*, 2013.
- [60] Muhammad Ibrahim, Naveed Akhtar, Saeed Anwar, Michael Wise, and Ajmal Mian. Perth-wa localization dataset in 3d point cloud maps, 2023.
- [61] NASA JPL and NGA. SRTM 30m Global 1 arc second V003, 2013.



reconstruction, and geospatial machine learning.



His research interests include LiDAR 3D point cloud acquisition and pre-processing, LiDAR-based point cloud signal processing and spatial modeling, geo-registration of unstructured data, as well as multispectral remote sensing technologies and precision agriculture.



His research interests include LiDAR 3D point cloud acquisition and pre-processing, LiDAR-based point cloud signal processing and spatial modeling, geo-registration of unstructured data, as well as multispectral remote sensing technologies and precision agriculture.



include computer vision, pattern classification, and cyber-physical systems.



Distinguished Speaker, the President of the Australian Pattern Recognition Society and IEEE Senior Member.

Xinyu Wang received the B.I.T. degree in Networking and Cybersecurity from the University of South Australia, in 2018, and the B.Sc. (Hons.) degree and the Master of Information Technology degree from The University of Western Australia (UWA) in 2024. He is currently pursuing the Ph.D. degree in Computer Science at UWA, beginning in 2025. He is working as a research officer and a casual teaching staff at UWA. His research interests include 3D point cloud processing, LiDAR-based spatial modeling, geo-referencing of unstructured data, urban scene

Muhammad Ibrahim received the B.Sc. degree in Computer Systems Engineering from the University of Engineering and Technology (UET), Peshawar, Pakistan, in 2008, and the M.Sc. degree in Personal Mobile and Satellite Communication from the University of Bradford, U.K., in 2010. He received the Ph.D. degree in Computer Science from The University of Western Australia (UWA), Australia, in 2023. He is currently a Research Scientist at the Department of Primary Industries and Regional Development (DPIRD), WA, and an Adjunct Research Fellow with UWA. He previously served as an Assistant Professor at FAST–National University of Computer and Emerging Sciences (NUCES), Pakistan. His research interests include semantic segmentation of 3D point clouds, remote sensing, LiDAR-based scene understanding, intelligent transportation, precision agriculture, localization and mapping, and deep learning across multi-modal geospatial datasets.

Haitian Wang received the B.Eng. degree in Internet of Things Engineering from Northwestern Polytechnical University, Xi’an, China, in 2019, and the M.Eng. degree in Computer Technology from Northwestern Polytechnical University in 2022. He received the MPE (Software) degree from the University of Western Australia in 2024. He is currently a Research Scientist in the Department of Primary Industries and Regional Development (DPIRD), Western Australia, and serves as a Research Officer and casual teaching Staff at UWA.

Atif Mansoor is an Assistant Professor with the Department of Computer Science and Software Engineering, University of Western Australia. Before joining The University of Western Australia, he taught at the National University of Sciences and Technology and Punjab University in Pakistan. He was an Erasmus Mundus scholar with the Norwegian University of Science and Technology, Gjøvik and Jean Monnet University, Saint-Etienne, France. He has published more than 70 papers in international conferences and journals. His research interests include computer vision, pattern classification, and cyber-physical systems.

Ajmal Mian is currently a Professor of Computer Science with The University of Western Australia, Perth, WA, Australia. He has received several major research grants from the Australian Research Council (ARC), the National Health and Medical Research Council of Australia, and the U.S. Department of Defense. His research interests include computer vision, machine learning, and artificial intelligence. Prof. Mian is an Australian Research Council Future Fellow, an International Association for Pattern Recognition (IAPR) Fellow, an ACM